

## Article

# Pyridyl-Thioethers as Capping Ligands for the Design of Heteroleptic Fe(II) Complexes with Spin-Crossover Behavior

Ökten Üngör <sup>1</sup>, Dilyara Igimbayeva <sup>1,2</sup>, Alina Dragulescu-Andrasi <sup>3</sup>, Sandugash Yergeshbayeva <sup>1</sup>, Teresa Delgado <sup>4</sup>, Samuel M. Greer <sup>1,5</sup>, Gabrielle Donalson <sup>1,6</sup>, Minyoung Jo <sup>1</sup>, Rakhmetulla Erkasov <sup>2</sup>, and Michael Shatruk <sup>1,5,\*</sup>

- <sup>1</sup> Department of Chemistry and Biochemistry, Florida State University, 95 Chieftan Way, Tallahassee, FL 32306, USA; ou15@my.fsu.edu (Ö.Ü.); dilya92-22@mail.ru (D.I.); sy18t@my.fsu.edu (S.Y.); sgreer@lanl.gov (S.M.G.); gabby\_donalson@yahoo.com (G.D.); mj13h@my.fsu.edu (M.J.)
- <sup>2</sup> Department of Chemistry, L.N. Gumilyov Eurasian National University, 5 Munaitpasov Str., Astana 010008, Kazakhstan; erkass@mail.ru
- <sup>3</sup> Department of Chemistry, University of Idaho, Moscow, ID 83844, USA; aandrasi@uidaho.edu
- <sup>4</sup> Département de Chimie Physique, Université de Genève, Quai Ernest Ansermet, 30, 1211 Genève, Switzerland; MariaTeresa.DelgadoPerez@unige.ch
- <sup>5</sup> National High Magnetic Field Laboratory, 1800 E Paul Dirac Dr, Tallahassee, FL 32310, USA
- <sup>6</sup> Department of Physical & Environmental Sciences, Colorado Mesa University, 1100 North Ave., Grand Junction, CO 81501, USA
- \* Correspondence: shatruk@chem.fsu.edu



**Citation:** Üngör, Ö.; Igimbayeva, D.; Dragulescu-Andrasi, A.; Yergeshbayeva, S.; Delgado, T.; Greer, S.M.; Donalson, G.; Jo, M.; Erkasov, R.; Shatruk, M. Pyridyl-Thioethers as Capping Ligands for the Design of Heteroleptic Fe(II) Complexes with Spin-Crossover Behavior. *Magnetochemistry* **2021**, *7*, 134. <https://doi.org/10.3390/magnetochemistry7100134>

Academic Editor: Greg A. Brewer

Received: 26 June 2021

Accepted: 13 September 2021

Published: 1 October 2021

**Publisher's Note:** MDPI stays neutral with regard to jurisdictional claims in published maps and institutional affiliations.



**Copyright:** © 2021 by the authors. Licensee MDPI, Basel, Switzerland. This article is an open access article distributed under the terms and conditions of the Creative Commons Attribution (CC BY) license (<https://creativecommons.org/licenses/by/4.0/>).

**Abstract:** Mononuclear heteroleptic complexes [Fe(tpma)(bimz)](ClO<sub>4</sub>)<sub>2</sub> (**1a**), [Fe(tpma)(bimz)](BF<sub>4</sub>)<sub>2</sub> (**1b**), [Fe(bpte)(bimz)](ClO<sub>4</sub>)<sub>2</sub> (**2a**), and [Fe(bpte)(bimz)](BF<sub>4</sub>)<sub>2</sub> (**2b**) (tpma = tris(2-pyridylmethyl)amine, bpte = *S,S'*-bis(2-pyridylmethyl)-1,2-thioethane, bimz = 2,2'-biimidazoline) were prepared by reacting the corresponding Fe(II) salts with stoichiometric amounts of the ligands. All complexes exhibit temperature-induced spin crossover (SCO), but the SCO temperature is substantially lower for complexes **1a** and **1b** as compared to **2a** and **2b**, indicating the stronger ligand field afforded by the N<sub>2</sub>S<sub>2</sub>-coordinating bpte ligand relative to the N<sub>4</sub>-coordinating tpma. Our findings suggest that ligands with mixed N/S coordination can be employed to discover new SCO complexes and to tune the transition temperature of known SCO compounds by substituting for purely N-coordinating ligands.

**Keywords:** spin crossover; thioether ligands; heteroleptic complexes; Mössbauer spectroscopy

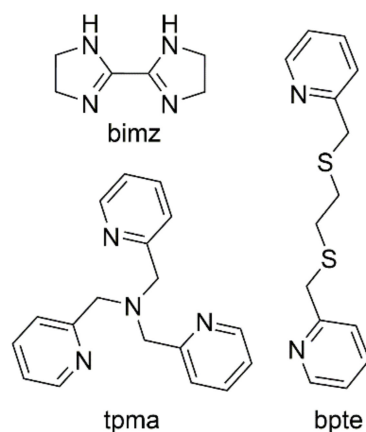
## 1. Introduction

The design of coordination environments for achieving reversible spin-state switching (spin crossover, SCO) in transition metal complexes is an interesting endeavor that crosses the boundaries between inorganic, organic, and physical chemistry. It is directly related to the discovery of magnetically bistable materials, as well as to the synthesis of new ligands and evaluation of relative stabilities of the low-spin (LS) and high-spin (HS) electronic configurations. While there are many examples of SCO among complexes of 3d metal ions, the majority of them (>90%) are represented by Fe(II) complexes [1]. In turn, the majority of the SCO Fe(II) complexes feature the metal ion in the {N<sub>6</sub>} coordination environment [2]. In order to expand the possibilities in the design of SCO complexes, it is important to find alternative coordination environments that can provide the appropriate ligand field strength for the occurrence of SCO.

In recent years, our and other groups have reported SCO in several Fe(II) complexes with the {N<sub>4</sub>S<sub>2</sub>} coordination, in which the S-donor atoms are provided by thioether functionalities [3–11]. In general, one thinks of thioethers as rather weak ligands, and initially we were quite surprised by the observation of SCO in such coordination environment. Nevertheless, the use of Mössbauer spectroscopy unequivocally confirmed the conversion between the LS and HS states of the Fe(II) ion in these complexes [5]. Another interesting

aspect of such complexes is the large change in the Fe–S bond length ( $\sim 0.3$  Å) that takes place upon conversion between the LS and HS structures, due to population of the anti-bonding  $e_g$ -orbitals in the HS state. In comparison, the typical change in the Fe–N bond lengths is  $\sim 0.2$  Å [12,13]. Thus, the SCO in the complexes with the  $\{N_4S_2\}$  coordination may also result in larger structural changes propagated through the crystalline lattice. These findings and considerations suggest new possibilities in the synthesis of SCO materials and their spin-state switching behavior.

To obtain further insight into the potency of thioether-containing ligands, we performed a comparative study of Fe(II) complexes containing ligands with and without S-donor atoms (Scheme 1). To that end, we used tetradentate ligands *S,S'*-bis(2-pyridylmethyl)-1,2-thioethane (bpte) and tris(2-pyridylmethyl)amine (tpma), which had been shown to afford heteroleptic SCO complexes with the Fe(II) ion [3–5,14–17]. Our study of heteroleptic complexes  $[\text{Fe}(\text{bpte})(\text{bim})]\text{X}_2$  ( $\text{bim} = 2,2'$ -biimidazole;  $\text{X} = \text{ClO}_4^-$ ,  $\text{BF}_4^-$ ,  $\text{OTf}^-$ ) [7] revealed that they exhibit SCO at much higher temperatures ( $>300$  K) as compared to the SCO in the analogous complexes with tpma ( $\sim 200$  K) [15]. The homoleptic complex  $[\text{Fe}(\text{bim})_3]^{2+}$  is known to exhibit only HS behavior [18], but combining the bidentate bim with the tetradentate bpte or tpma consistently leads to SCO in the heteroleptic complexes mentioned above. On the other hand, a hydrogenated derivative of bim, 2,2'-biimidazoline (bimz), affords a homoleptic Fe(II) complex that shows SCO around 110 K [19]. The  $[\text{Fe}(\text{bimz})_3]^{2+}$  cation, however, is quite air-sensitive in solution, as well as in the solid state. All these considerations have prompted us to synthesize and investigate heteroleptic complexes  $[\text{Fe}(\text{tpma})(\text{bimz})]\text{X}_2$  (**1a**:  $\text{X} = \text{ClO}_4^-$ ; **1b**:  $\text{X} = \text{BF}_4^-$ ) and  $[\text{Fe}(\text{bpte})(\text{bimz})]\text{X}_2$  (**2a**:  $\text{X} = \text{ClO}_4^-$ ; **2b**:  $\text{X} = \text{BF}_4^-$ ). Herein, we demonstrate that the former complexes exhibit SCO below 300 K, while the latter show SCO only 300 K. Thus, we confirm once again that bpte is a stronger ligand than tpma, and the mixed N,S-coordinating ligands with thioether functionalities provide a promising platform for the discovery of new SCO materials.



**Scheme 1.** Ligands used in this work.

## 2. Results

### 2.1. Synthesis

Complexes **1a**, **1b**, **2a**, and **2b** were synthesized by reacting Fe(II) perchlorate or tetrafluoroborate salts first with the bidentate ligand (bimz) and then with the tetradentate ligand (tpma or bpte) in a MeOH–EtOH solvent mixture. We found such sequential addition to be the most effective, resulting in good yields of the target heteroleptic complexes. Despite the low solubility of bimz and the resulting complexes in the reaction solvent, this method yields rather pure precipitates of **1a–2b**, which can be conveniently recrystallized from MeCN–Et<sub>2</sub>O. The complexes are sufficiently air-stable in the solid state, but should be kept in a desiccator for prolonged storage. The only exception was observed for complex **1a**, in which case the sample tended to develop a small amount of an Fe(III) impurity upon storage, as will be shown by Mössbauer spectroscopy below.

## 2.2. Crystal Structures

Single-crystal X-ray diffraction confirmed that compounds **1a–2b** crystallize as mononuclear heteroleptic complexes. The Fe<sup>II</sup> ion resides in a distorted octahedral coordination environment formed by one tpma and one bimz ligand in **1a** and **1b** and by one bpte and one bimz ligand in **2a** and **2b** (Figure 1). All crystal structures are solvent-free, except for that of **2a**, which contains an interstitial acetonitrile molecule.

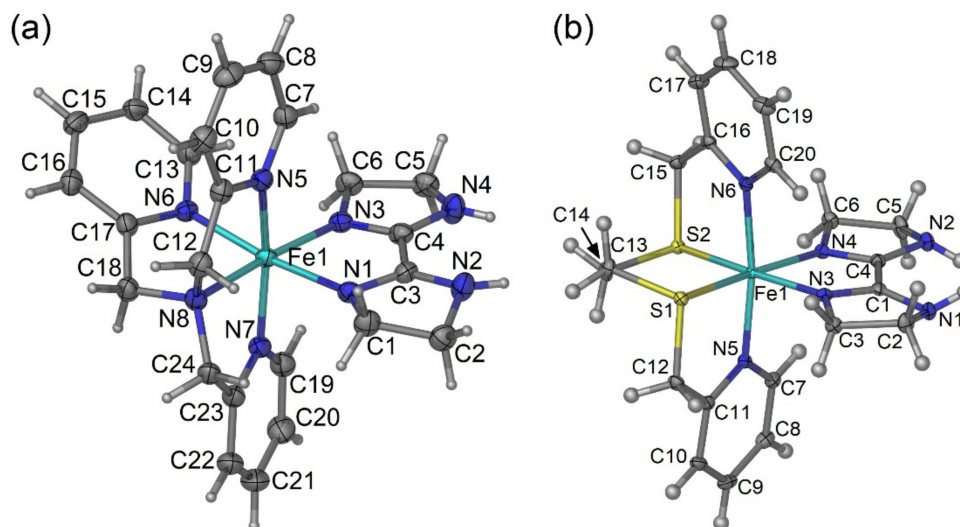


**Figure 1.** The  $[\text{Fe}(\text{tpma})(\text{bimz})]^{2+}$  (a) and  $[\text{Fe}(\text{bpte})(\text{bimz})]^{2+}$  (b) cations in the crystal structures of **1b** and **2a**·CH<sub>3</sub>CN, respectively. The thermal ellipsoids are shown at 50% probability level.

The TGA analysis of a freshly filtered sample of **2a** revealed ~2.5% mass loss when the sample was heated to 340 K (67 °C). This mass loss corresponds to ~0.4 molecule of MeCN per formula unit, which is lower than the solvent content determined by the crystal structure determination, **2a**·MeCN. This observation indicates that the interstitial MeCN molecules are lost immediately from the sample of **2a** if it is not covered with mother liquid. Indeed, the elemental analysis performed on the solids stored for several days after filtration indicated the lack of interstitial solvent molecules in sample **2a**, as well as in the other three samples (see the Section 4).

Examination of metric parameters for the structures determined at different temperatures (Table 1) revealed that the Fe–N bonds in structure **1b** undergo substantial elongation when the temperature is increased from 100 to 230 K. The bond lengths at 100 K are characteristic of the LS Fe<sup>II</sup> ion while the ones at 230 K approach typical values for the HS Fe<sup>II</sup> ion [20]. The octahedral distortion parameter  $\Sigma_{90}$ , defined as the sum of absolute deviations of 12 *cis*-N–Fe–N angles from the ideal octahedral value of 90°, also exhibits a large increase at higher temperature. These changes indicate that complex **1b** undergoes thermally driven SCO.

Complex **1a** exhibits much smaller changes in the Fe–N bond lengths. This structure contains two unique Fe sites in the asymmetric unit, and for both of them the Fe–N distances observed at 230 K are typical of the HS Fe<sup>II</sup> ion. The Fe–N distances observed at 90 K are only slightly smaller, while the  $\Sigma_{90}$  values remain nearly the same at both temperatures.

In contrast to **1b**, the crystal structure parameters of **2a** and **2b** remain almost unchanged between 100 and 230 K, with only a negligible increase in the bond lengths associated with thermal expansion of the lattice. The Fe–N and Fe–S distances are consistent with the LS Fe<sup>II</sup> ions, based on the comparison to the bond lengths in the {N<sub>4</sub>S<sub>2</sub>}-coordinated complexes that exhibit SCO [5].

It is also interesting to compare the octahedral distortion parameter  $\Sigma_{90}$  observed for the  $[\text{Fe}(\text{L}_4)(\text{bimz})]^{2+}$  cations described in this work to the  $\Sigma_{90}$  values in the previously reported  $[\text{Fe}(\text{L}_4)(\text{bim})]^{2+}$  cations. The SCO complex  $[\text{Fe}(\text{tpma})(\text{bim})](\text{ClO}_4)_2$  showed

$\Sigma_{90} = 59.9^\circ$  in the LS state and  $95.1^\circ$  in the HS state [15], while the corresponding values found for  $[\text{Fe}(\text{tpma})(\text{bimz})](\text{BF}_4)_2$  (**1b**) are substantially larger,  $79.5(5)^\circ$  at 100 K and  $114.4(2)^\circ$  at 230 K. Likewise, in  $[\text{Fe}(\text{bpte})(\text{bim})]\text{X}_2$  complexes, both of which are LS at 230 K, the values of  $\Sigma_{90}$  are  $39.2^\circ$  for  $\text{X} = \text{ClO}_4^-$  and  $43.0^\circ$  for  $\text{X} = \text{BF}_4^-$  [7], while in  $[\text{Fe}(\text{bpte})(\text{bimz})]\text{X}_2$  these values increase to  $45.2(2)^\circ$  in **2a** and  $54.4(2)^\circ$  in **2b**, respectively. These comparisons clearly demonstrate that the coordination environment of the  $\text{Fe}^{\text{II}}$  ion in the bimz-containing complexes becomes more distorted due to the non-aromatic, non-planar structure of the bimz ligand. At the same time, the distortion from the ideal octahedral coordination is smaller in the complexes with bpte as compared to those with tpma, which might in part contribute to the greater stability of the LS state in the former (see below).

**Table 1.** Selected bond lengths and angles in crystal structures of **1a**, **1b**, **2a**· $\text{CH}_3\text{CN}$ , and **2b**.

Complex	<b>1a</b> <sup>a</sup>		<b>1b</b>		<b>2a</b> · $\text{CH}_3\text{CN}$		<b>2b</b>	
	90	230	100	230	100	230	100	230
Bond lengths, Å								
Fe–N <sub>tpma</sub> (amine)	Fe1: 2.262(3) Fe2: 2.240(3)	2.269(3) 2.256(3)	2.004(4)	2.189(2)	–	–	–	–
Fe–N <sub>tpma</sub> (pyridyl) <sup>b</sup>	Fe1: 2.178(3) Fe2: 2.184(3)	2.187(3) 2.198(3)	1.989(4)	2.149(2)	–	–	–	–
Fe–N <sub>bimz</sub> (1) <sup>b</sup>	Fe1: 2.159(3) Fe2: 2.145(3)	2.165(3) 2.155(3)	2.034(4)	2.138(2)	1.983(2)	1.989(2)	2.008(3)	2.009(2)
Fe–N <sub>bpte</sub> <sup>b</sup>	–	–	–	–	2.006(2)	2.007(2)	2.032(2)	2.033(2)
Fe–S(1) <sup>a</sup>	–	–	–	–	2.2402(7)	2.2408(6)	2.2668(9)	2.2678(7)
$\Sigma_{90}(\text{cis-N/S-Fe-N/S})$ , deg	Fe1: 113.5(1) Fe2: 108.8(1)	Fe1: 111.1(1) Fe2: 110.0(1)	79.5(5)	114.4(2)	44.5(2)	45.2(2)	54.4(3)	54.4(2)

<sup>a</sup> The asymmetric unit contains two unique metal sites, Fe(1) and Fe(2); <sup>b</sup> An average of the corresponding bond lengths.

In the crystal structure of **1a**, the  $[\text{Fe}(\text{tpma})(\text{bimz})]^{2+}$  cations form layers separated by the  $\text{ClO}_4^-$  anions (Figure 2a). The interlayer interactions between the cations are weak. The layers are parallel to the (110) planes of the lattice. Within each layer, one of the imidazoline rings of the bimz ligand engages in a  $\pi$ - $\pi$  interaction with a pyridyl ring of the tpma ligand from an adjacent complex, and such interactions create a chain pattern (Figure 2b). The other imidazoline ring of bimz is involved in weaker  $\sigma$ - $\pi$  interactions with a tpma pyridyl ring from the neighbor chain.

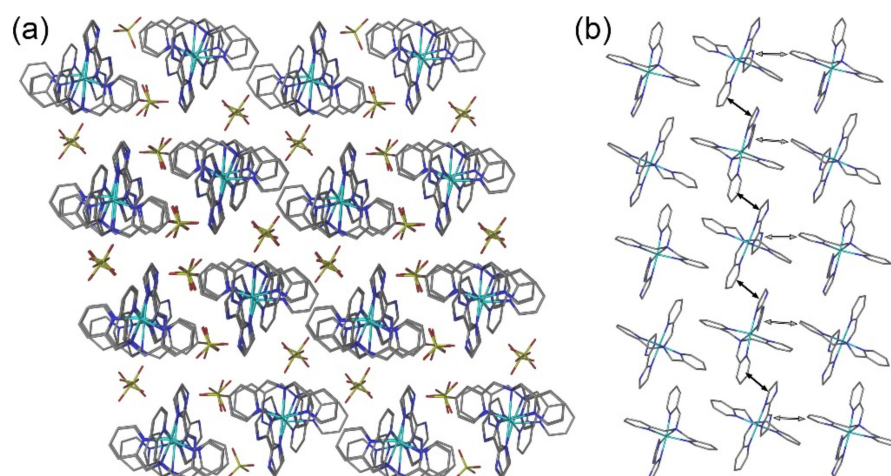


**Figure 2.** Crystal packing of **1a**: a side view of four layers of  $[\text{Fe}(\text{tpma})(\text{bimz})]^{2+}$  cations (**a**) and a top view of one layer (**b**). The  $\pi$ - $\pi$  and  $\sigma$ - $\pi$  contacts are indicated with black and gray arrows, respectively. Color scheme: Fe = cyan, Cl = yellow, O = red, N = blue, C = gray. Hydrogen atoms are omitted for clarity.

The crystal packing of **1b** can be described as chains of  $[\text{Fe}(\text{tpma})(\text{bimz})]^{2+}$  cations arranged parallel to the  $c$  axis, with the  $\text{BF}_4^-$  anions separating the chains (Figure 3a). The structural arrangement is quite different from the one observed for **1a**. Within each chain, the adjacent cations exhibit  $\pi$ - $\pi$  interactions between an imidazoline ring of bimz and a pyridyl ring of tpma (Figure 3b). In addition, less pronounced  $\sigma$ - $\pi$  interactions are observed between C-H groups of the other imidazoline ring of bimz and one of the remaining pyridyl rings of tpma.

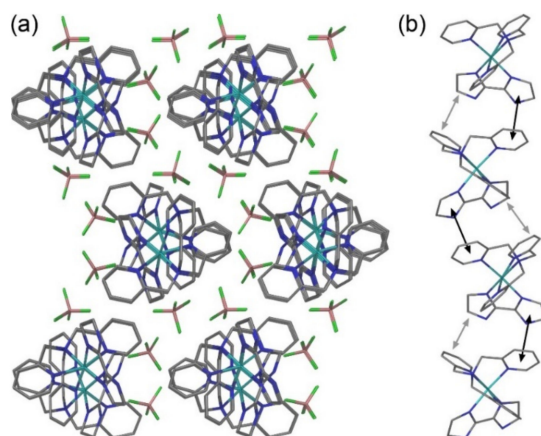


**Figure 3.** Crystal packing of **1b**: a top view of chains of  $[\text{Fe}(\text{tpma})(\text{bimz})]^{2+}$  cations (a) and a side view of one chain (b). The  $\pi$ - $\pi$  and  $\sigma$ - $\pi$  contacts within the chain are indicated with black and gray arrows, respectively. Color scheme: Fe = cyan, F = green, O = red, N = blue, C = gray, B = coral. Hydrogen atoms are omitted for clarity.

The crystal packing of **2a**· $\text{CH}_3\text{CN}$  reveals columns of  $[\text{Fe}(\text{bpte})(\text{bimz})]^{2+}$  cations arranged parallel to the  $c$  axis, with the  $\text{ClO}_4^-$  anions and  $\text{CH}_3\text{CN}$  molecules separating the columns (Figure 4a). Each  $[\text{Fe}(\text{bpte})(\text{bimz})]^{2+}$  cation in the column interacts with two neighbor cations via  $\pi$ - $\pi$  contacts between imidazoline rings, with the interplanar spacing of  $\sim 3.49$  Å (Figure 4b). Interactions between the columns occur via  $\sigma$ - $\pi$  contacts between ethylene fragments and pyridyl rings of neighbor bpte ligands.

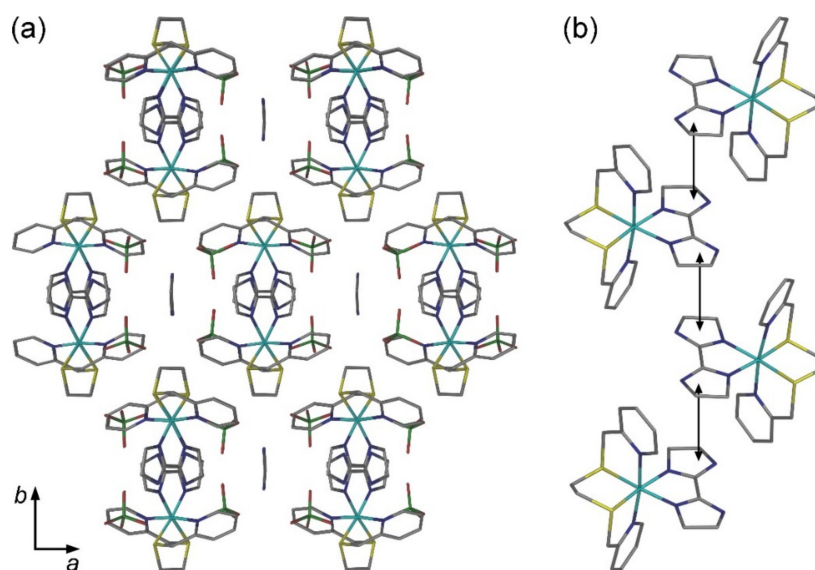


**Figure 4.** (a) The crystal packing of **2a**· $\text{CH}_3\text{CN}$  viewed down the  $c$  axis, showing the top view of the columns of  $[\text{Fe}(\text{bpte})(\text{bimz})]^{2+}$  cations. (b) A side view of the column of cations, emphasizing the  $\pi$ - $\pi$  interactions between imidazoline rings. Color scheme: Fe = cyan, Cl = green, S = yellow, O = red, N = blue, C = gray. Hydrogen atoms are omitted for clarity.

In contrast to structures **1a**, **1b**, and **2a**·CH<sub>3</sub>CN, in which the assembly of cationic complexes into columns takes place via pronounced  $\pi$ - $\pi$  and  $\sigma$ - $\pi$  interactions, the structure of **2b** reveals the lack of any pronounced crystal packing features. In principle, one could distinguish columns of  $[\text{Fe}(\text{bpte})(\text{bimz})]^{2+}$  cations propagating along the *c* axis (Figure 5a), but only weak van-der-Waals interactions are observed between the cations, with the  $\text{BF}_4^-$  anions separating the chains. Perhaps the most interesting observation in the crystal packing of **2b** is the existence of van-der-Waals S··S contacts (3.58 Å) between the columns (Figure 5b).

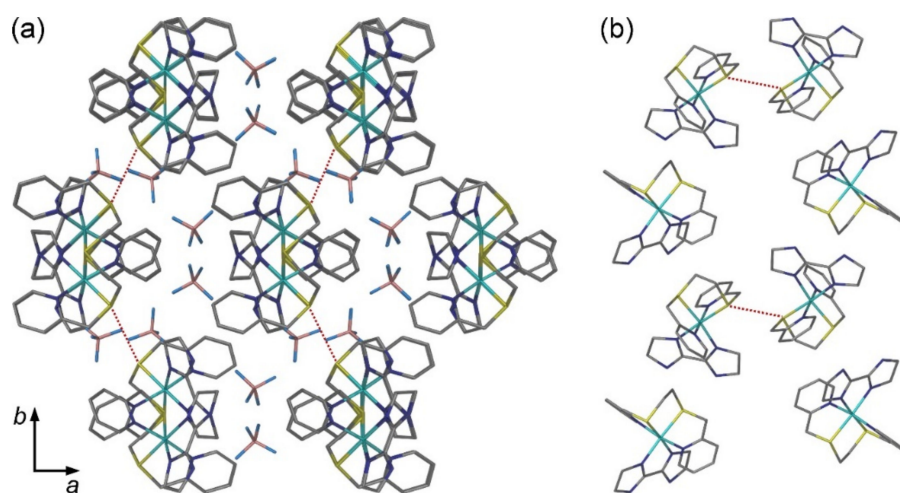


**Figure 5.** (a) The crystal packing of **2b** viewed down the *c* axis, showing the top view of the columns of  $[\text{Fe}(\text{bpte})(\text{bim})]^{2+}$  cations. (b) A side view of two columns of cations. The van-der-Waals S··S contacts between the columns are shown with red dotted lines. Color scheme: Fe = cyan, S = yellow, F = teal, N = blue, C = gray. Hydrogen atoms are omitted for clarity.

### 2.3. Magnetic Properties

Variable-temperature magnetic susceptibility measurements were carried out on polycrystalline samples of all four complexes. The temperature was varied at a rate of 1 K/min. For complex **1b**, a complete and gradual SCO is observed (Figure 6a). The  $\chi T$  value decreases from 3.06 emu·K/mol at 300 K to nearly zero below 130 K. The midpoint of SCO, at which the HS and LS fractions are equal ( $f_{\text{HS}} = f_{\text{LS}} = 0.5$ ), is observed at  $T_{1/2} = 175$  K. Such magnetic behavior is in agreement with the substantial change in the Fe–N bond lengths, which are indicative of the LS configuration at 100 K and the nearly complete HS configuration at 230 K (Table 1). A more gradual SCO was observed for complex **1a**. The room-temperature  $\chi T$  value of 3.43 emu·K/mol (Figure 6) is consistent with the presence of one HS Fe<sup>II</sup> ion per formula unit ( $S = 2$ ). The onset of SCO takes place below 180 K, but the decrease in the  $\chi T$  value is very gradual, and a plateau is observed below 70 K. The residual HS fraction of  $f_{\text{HS}} \sim 0.4$  was estimated from this plateau, indicating an incomplete SCO. This result can be explained by the kinetic effect, which “freezes” the SCO process due to the decreased energy of vibronic coupling between the SCO centers below  $\sim 60$ –70 K [5,21]. The decrease in the  $\chi T$  curve below 20 K is due to zero-field splitting. The slow decrease of the  $\chi T$  value below 180 K explains the rather small changes in the Fe–N bond lengths observed for the crystal structure of **1a** between 230 and 90 K (Table 1). The more abrupt SCO for complex **1b** can be attributed to the more efficient interactions between the cationic complexes along the columns observed in the crystal structures (cf. Figures 2 and 3).

In contrast to the complexes prepared with *tpma*, complexes **2a** and **2b** are characterized by much higher stability of the LS state. Upon warming up, an onset of SCO is observed only at 320 K for **2a** and at 350 K for **2b** (Figure 6). Thus, it appears that the increase in the ligand field strength due to the replacement of *tpma* with *bpte* shifts the SCO to substantially higher temperatures. Interestingly, complex **2a** exhibits an abrupt and complete spin transition with  $T_{1/2} = 330$  K, while complex **2b** also exhibits an abrupt

increase in  $\chi T$  at 360 K, but the change appears to correspond to ~25% of the Fe centers changing their spin state from LS to HS, hinting at the formation of a mixed LS/HS state. Such mixed states are not uncommon for SCO complexes, and their formation might be related to crystal structure transformations during the spin transition [12,22].

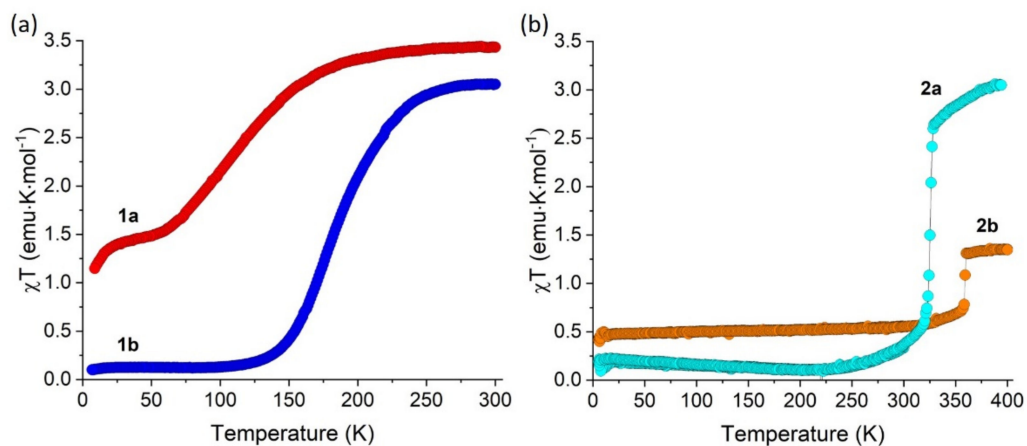


**Figure 6.** Temperature dependence of  $\chi T$  for complexes **1a** and **1b** (a) and **2a** and **2b** (b).

#### 2.4. Mössbauer Spectroscopy

Mössbauer spectra of **1a** and **1b** were collected at 80 and 250 K in zero applied magnetic field. The isomer shift ( $\delta$ ), quadrupole splitting ( $\Delta E_Q$ ), and linewidth ( $\Gamma_{L/R}$ ) parameters obtained by the spectral fitting procedure, as well as relative areas corresponding to various Fe species detected in the samples, are summarized in Table 2. The spectrum of **1a** obtained at 250 K (Figure 7a) exhibits a single quadrupole doublet with  $\delta = 1.00(4)$  mm/s and  $\Delta E_Q = 2.84(6)$  mm/s. These values are typical of the HS-Fe<sup>II</sup> ion [23]. In contrast, two quadrupole doublets were observed in the spectrum recorded at 80 K. The first one is again typical of the HS-Fe<sup>II</sup> species, with  $\delta = 1.07(2)$  mm/s and  $\Delta E_Q = 3.24(2)$  mm/s, while the second doublet, with  $\delta = 0.52(1)$  mm/s and  $\Delta E_Q = 0.51(2)$  mm/s, is indicative of the LS-Fe<sup>II</sup> ion [23]. The ratio between the LS and HS fractions is  $0.53(3):0.47(3) \approx 1:1$ , which is in agreement with the ratio evaluated from magnetic susceptibility data at this temperature (Figure 6).

**Table 2.** Parameters obtained by fitting Mössbauer spectra of complexes **1a** and **1b**.

Complex	T (K)	Site	$\delta$ (mm/s)	$\Delta E_Q$ (mm/s)	$\Gamma_{L/R}$ (mm/s)	Area (%)
<b>1a</b>	80	LS-Fe <sup>II</sup>	0.52(1)	0.51(2)	0.33(1)	53(3)
		HS-Fe <sup>II</sup>	1.07(2)	3.24(2)	0.31	47(3)
	250	HS-Fe <sup>II</sup>	1.00(4)	2.84(6)	0.41	100
<b>1b</b>	80	LS-Fe <sup>II</sup>	0.509(5)	0.598(5)	0.27	93(2)
		HS-Fe <sup>III</sup>	0.46(2)	1.47(2)	0.27	7(2)
	250	LS-Fe <sup>II</sup>	0.51(8)	0.56(8)	0.37	18(5)
		HS-Fe <sup>II</sup>	1.07(2)	2.82(2)	0.32/0.40	75(5)
		HS-Fe <sup>III</sup>	0.46(8)	1.47(8)	0.27	7(5)

In contrast, the Mössbauer spectrum of sample **1b** recorded at 80 K (Figure 7b) revealed the presence of Fe<sup>II</sup> ions only in the LS state, with  $\delta = 0.509(5)$  mm/s and  $\Delta E_Q = 0.598(5)$  mm/s being similar to those observed for the LS-Fe<sup>II</sup> species of **1a**. The Mössbauer spectrum of **1b**, however, also revealed the presence of 7% of an impurity phase, with the parameters characteristic of a dinuclear oxo-bridged Fe<sup>III</sup> complex. We carried out multiple experiments to eliminate this impurity, but it was persistently present in the bulk samples of **1b**, indicating that this complex, when prepared in a larger amount for

Mössbauer experiments, is susceptible to slight oxidation. The fraction of the ferric impurity remains unchanged in the spectrum of **1b** recorded at 250 K, while the dominant Fe<sup>II</sup> species exist as a mixture of HS-Fe<sup>II</sup> and LS-Fe<sup>II</sup> in ~4:1 ratio (Table 2). These observations are consistent with the magnetic behavior of **1b**, which reveals the onset of SCO from the HS to LS state upon cooling below ~275 K and the complete conversion to the LS state below 120 K (Figure 6a).

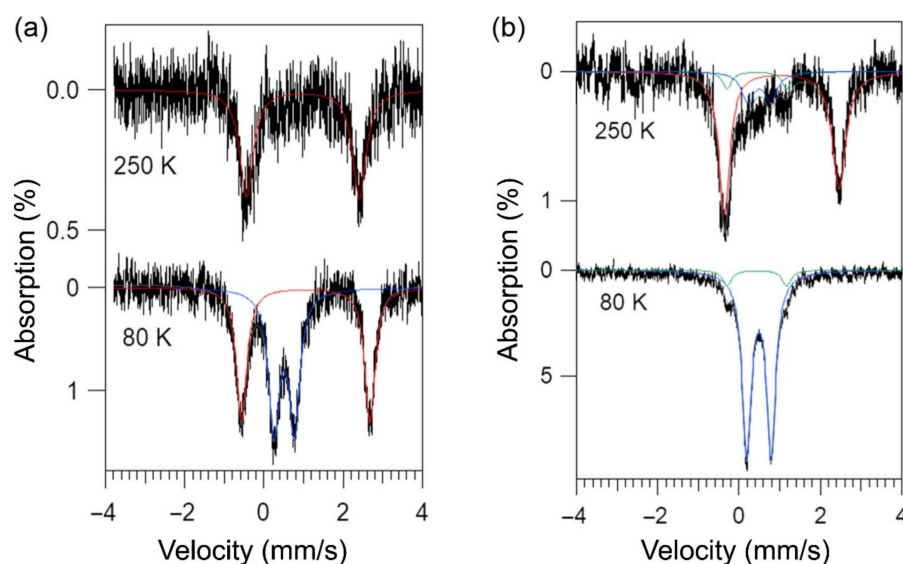


**Figure 7.** Zero-field <sup>57</sup>Fe Mössbauer spectra of **1a** (a) and **1b** (b) recorded at 250 and 80 K in zero applied magnetic field. The spectral components corresponding to the HS and LS states are shown with solid red and blue curves, respectively. In the case of **1b**, the ferric impurity is indicated with a solid green curve. The total spectral simulation is traced with a solid gray line.

Mössbauer studies on complexes **2a** and **2b** were not pursued, due to the limitation of our instrument that did not allow probing the range of SCO temperatures (above 300 K) observed for these compounds.

### 2.5. LIESST Effect in Complex **1b**

SCO complexes that exhibit complete thermally driven spins-state conversion below 300 K frequently show light-induced conversion from the ground LS state to the metastable HS state at low temperatures, a phenomenon known as light-induced excited spin state trapping (LIESST) [24]. While the high temperatures of SCO observed for complexes **2a** and **2b** are not conducive to the LIESST behavior, and complex **1a** shows a rather gradual and incomplete SCO, the slightly more abrupt and complete SCO with  $T_{1/2} = 175$  K, observed in the magnetic behavior of **1b**, prompted us to study the possibility of LIESST in this complex. The optical absorption spectra were recorded on a single crystal of **1b** of ~100 μm thickness in the range from 475 to 800 nm. At room temperature, when the sample is in the HS state, a relatively weak absorption band centered at 600 nm was observed, with an extinction coefficient of 30 M<sup>-1</sup> cm<sup>-1</sup> according to the optical density (the black line in Figure 8a). As the temperature was decreased, the intensity of this band increased and maximized at 6 K in the LS state. Hence, this band corresponds to the <sup>1</sup>A<sub>1</sub> → <sup>1</sup>T<sub>1</sub> *d-d* transition of the LS state. A tail of the much more intense metal-to-ligand-charge-transfer (MLCT) band was observed at higher energies in the HS state whereas this band saturated at wavelengths below 550 nm in the LS state.

Once the spectra of both the HS and LS states were obtained, the LIESST effect was probed by irradiating the crystal at 6 K. First, the crystal was irradiated with a 532 nm laser operating at 2 mW mm<sup>-2</sup>. After 5 min of irradiation, the LS → HS conversion achieved only 3.3%, based on the change in the optical density at 600 nm (the green line). Neither longer irradiation times nor a higher laser power improved the conversion. However, by

employing a longer wavelength laser, with 650 nm and 2 mW mm<sup>-2</sup>, a higher conversion was achieved after 5 min (the brown line) due to the improved penetration depth. The conversion further increased under longer irradiation times, reaching a maximum value of 32% after 150 min (the red line).

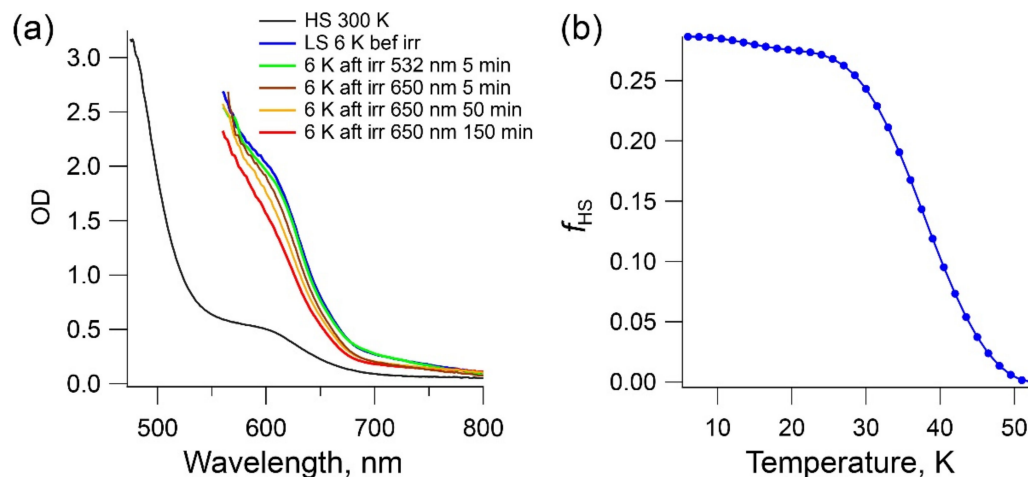


**Figure 8.** (a) Optical absorption spectra recorded on a single crystal of **1b** at room temperature and 6 K before and after photo-excitation. The variation in the *d-d* absorption band of the LS state under different excitation wavelengths and times is shown. (b) The change in the fraction of the HS state as a function of temperature upon heating from 6 K at 0.3 K min<sup>-1</sup>.

The stability of the LIESST state was studied by heating the sample at 0.3 K min<sup>-1</sup> after irradiation. A gradual HS→LS relaxation was observed above 30 K, with the complete recovery of the LS ground state at 50 K (Figure 8b). Thus, while complex **1b** exhibits the LIESST behavior, the stability of the photoinduced HS state is rather low, as compared, for example, to the related complex [Fe(tpma)(xbim)](ClO<sub>4</sub>)<sub>2</sub> (xbim = 1,1'-( $\alpha,\alpha'$ -*o*-xylyl)-2,2'-biimidazole) [15]. This might be explained by the lower cooperativity of intermolecular interactions and less rigid structure of the bidentate ligand in the structure of **1b**.

### 3. Conclusions

The comparative study of SCO behavior in a series of heteroleptic Fe(II) complexes with the bidentate ligand, bimz, and a tetradentate ligand, either tpma or bpte, demonstrates the stronger ligand field of the N<sub>2</sub>S<sub>2</sub>-coordinating bpte as compared to the N<sub>4</sub>-coordinating tpma. The SCO in the tpma-containing complexes occurs below 300 K, while in the bpte-containing complexes the SCO is observed above 300 K. These findings agree with our earlier observation of substantially higher SCO temperatures in heteroleptic Fe(II) complexes that combine biimidazole-type ligands and bpte as compared to analogous complexes with tpma. Besides, partial LS→HS photoconversion based on the LIESST effect has been proven for one of the tpma-containing complexes.

This work clearly demonstrates that ligands combining pyridyl and thioether functionalities create a rather strong ligand field at the metal center. It should be pointed out, however, that tpma and bpte do not bear exact topological equivalence, since tpma has a tripodal metal-coordinating skeleton while bpte has a linear skeleton. A more accurate comparison would be offered by investigating complexes of bpte relative to complexes of *N,N'*-bis(2-pyridylmethyl)-1,2-ethanediamine [25]. Such studies, as well as studies of other N/S-coordinating ligands for the synthesis of SCO complexes, are currently under way in our labs, and their results will be reported in due course.

### 4. Materials and Methods

**Synthesis.** All reactions were performed under an inert N<sub>2</sub> atmosphere using standard Schlenk techniques. All reagents and anhydrous solvents were purchased from Millipore

Sigma and used as received. Ligands tpma [26], bpte [27], and bimz [28] were synthesized according to the published procedures. Anhydrous commercial solvents were additionally purified by passing through a double-stage drying/purification system (Pure Process Technology, Nashua, NH, USA). Elemental analyses were performed by Atlantic Microlab, Inc. (Norcross, GA, USA).

**Caution:** Complexes between metal ions and organic ligands with perchlorate anions are potentially explosive. The compounds should be prepared in small amounts and handled with great care!

**[Fe(tpma)(bimz)](ClO<sub>4</sub>)<sub>2</sub> (1a).** A yellow solution of Fe(ClO<sub>4</sub>)<sub>2</sub>·6H<sub>2</sub>O (72.6 mg, 0.200 mmol) in 2 mL of methanol (MeOH) was added to a suspension of bimz (27.6 mg, 0.200 mmol) in 8 mL of ethanol (EtOH). The resulting orange suspension was stirred for ca. 30 s, followed by the addition of a solution of tpma (58.0 mg, 0.200 mmol) in 2 mL of MeOH. The mixture was stirred vigorously for 30 min. The resulting dark orange-brown solution was filtered under inert atmosphere, and the filtrate was layered with 8 mL of diethyl ether and left undisturbed. Orange crystals that formed after several days were recovered by filtration, washed successively with cold MeOH (1 mL) and diethyl ether (Et<sub>2</sub>O, 1 mL), and dried by suction. Yield = 51.2 mg (37.5%). *Elem. analysis:* calcd. (found) for FeCl<sub>2</sub>O<sub>8</sub>N<sub>8</sub>C<sub>24</sub>H<sub>28</sub> (1a): C, 42.19 (41.74); H, 4.13 (4.45); N, 16.40 (16.43).

**[Fe(tpma)(bimz)](BF<sub>4</sub>)<sub>2</sub> (1b).** A yellow solution of Fe(BF<sub>4</sub>)<sub>2</sub>·6H<sub>2</sub>O (67.6 mg, 0.200 mmol) in 2 mL of MeOH was added to a suspension of bimz (27.6 mg, 0.200 mmol) in 8 mL of EtOH. The resulting orange suspension was stirred for ca. 30 s, followed by the addition of a solution of tpma (58.0 mg, 0.200 mmol) in 2 mL of MeOH. The reaction mixture was stirred vigorously for 30 min. An orange precipitate that formed was recovered by filtration and dissolved in 6 mL of acetonitrile (MeCN). The resulting solution was layered with 8 mL of Et<sub>2</sub>O. Orange crystals that formed after several days were recovered by filtration, washed successively with cold MeOH (1 mL) and Et<sub>2</sub>O (1 mL), and dried by suction. Yield = 81.7 mg (62.1%). *Elem. analysis:* calcd. (found) for FeB<sub>2</sub>F<sub>8</sub>N<sub>8</sub>C<sub>24</sub>H<sub>28</sub> (1b): C, 43.81 (44.06); H, 4.29 (4.22); N, 17.03 (17.01).

**[Fe(bpte)(bimz)](ClO<sub>4</sub>)<sub>2</sub> (2a).** Complex 2a was prepared in the same manner as complex 1b, starting with 72.6 mg (0.200 mmol) of Fe(ClO<sub>4</sub>)<sub>2</sub>·6H<sub>2</sub>O, 27.6 mg (0.200 mmol) of bimz, and 55.3 mg (0.200 mmol) of bpte. Yield = 87.6 mg (61.7%). *Elem. analysis:* calcd. (found) for FeCl<sub>2</sub>O<sub>8</sub>N<sub>6</sub>C<sub>20</sub>H<sub>26</sub>S<sub>2</sub> (2a): C, 35.89 (35.87); H, 3.92 (4.02); N, 12.56 (12.59).

**[Fe(bpte)(bimz)](BF<sub>4</sub>)<sub>2</sub> (2b).** Complex 2b was prepared in the same manner as complex 1b, starting with 67.6 mg (0.200 mmol) of Fe(BF<sub>4</sub>)<sub>2</sub>·6H<sub>2</sub>O, 27.6 mg (0.200 mmol) of bimz, and 55.3 mg (0.200 mmol) of bpte. Yield = 85.0 mg (66.0%). *Elem. analysis:* calcd. (found) for FeB<sub>2</sub>F<sub>8</sub>N<sub>6</sub>C<sub>20</sub>H<sub>26</sub>S<sub>2</sub> (2b): C, 37.30 (37.36); H, 4.07 (3.98); N, 13.05 (12.97).

**Magnetic Measurements.** Magnetic susceptibility measurements were carried out on polycrystalline samples, using a Magnetic Property Measurement System MPMS-XL (Quantum Design MPMS-XL) equipped with a superconducting quantum interference device (SQUID). Magnetic susceptibility was measured in a direct-current applied magnetic field of 1000 Oe in the 5–400 K temperature range, at cooling and heating rates of 1 K/min. The data were corrected for the diamagnetic contribution from the sample holder and for the intrinsic diamagnetism using tabulated constants [29].

**Mössbauer Spectroscopy.** <sup>57</sup>Fe Mössbauer spectra were collected on a constant acceleration instrument at 80 and 250 K, under zero applied magnetic field. A polycrystalline sample was placed directly in a custom-made polyethylene cup and constrained with a tightly fitted stopper. Isomer shifts are quoted relative to an α-Fe metal foil at room temperature. The spectra were simulated with the MossA software [30].

**Optical Spectroscopy.** Optical measurements were performed on a single crystal of 1b (4.5 × 3.0 × 0.1 mm<sup>3</sup>) mounted on a copper plate to completely cover a small aperture drilled in the plate. The assembly was inserted into a cryostat (Janis-Sumitomo) capable of reaching 4 K. Full optical spectra were recorded in the absorption mode in the 475–800 nm range on a double beam spectrometer (Cary 5000). Investigation of light-induced spin-state conversion was performed by irradiating the sample at 6 K with a HeNe

laser (2 mW/mm<sup>2</sup>). Two irradiation wavelengths were used, 532 nm and 650 nm, and the latter was found to be optimal for the penetration depth and efficiency of the light-induced transformation. The fraction of the HS state ( $f_{\text{HS}}$ ) at any time  $t$  was evaluated from the Vegard's law:  $f_{\text{HS}}(t) = (\text{OD}_{\text{LS}} - \text{OD}_t) / (\text{OD}_{\text{LS}} - \text{OD}_{\text{HS}})$ , where  $\text{OD}_{\text{LS}}$  and  $\text{OD}_{\text{HS}}$  are optical densities at 600 nm measured for the pure LS and HS states, respectively, and  $\text{OD}_t$  is the optical density measured at the specific time at the same wavelength. The  $\text{OD}_{\text{LS}}$  and  $\text{OD}_{\text{HS}}$  values were obtained from the absorption spectra recorded for non-irradiated samples at 6 K and 300 K, respectively. The OD values were corrected from an eventual baseline jump or shift by taking the difference between the OD at 600 nm and the OD at 800 nm, where no noticeable absorption bands occurred in the two states.

**X-ray Crystallography.** Single-crystal X-ray diffraction was performed on a Bruker APEX-II diffractometer equipped with a CCD detector or on a Rigaku-Oxford Diffraction Synergy-S diffractometer equipped with a HyPix detector. A graphite-monochromated Mo- $K\alpha$  radiation source ( $\lambda = 0.71073 \text{ \AA}$ ) was used in each case. In a typical experiment, a single crystal was suspended in Paratone-N oil (Hampton Research) and mounted on a cryoloop, which was cooled to the desired temperature in an N<sub>2</sub> cold stream. The data set was recorded as  $\omega$ -scans at 0.3–0.5° step width and integrated with the Bruker SAINT [31] or CrysAlis [32] software package. A multi-scan adsorption correction was applied based on multiple equivalent measurements (SADABS) [33]. The space group was determined with XPREP [34], and the crystal structure solution and refinement were carried out using the SHELX software [35]. The final refinement was performed with anisotropic atomic displacement parameters for all non-hydrogen atoms. All H atoms were placed in calculated positions and refined in the riding model, except for the N-bound H atoms of bimz, which were located on the difference Fourier electron density map and refined in the riding model. Full details of the crystal structure refinement and the final structural parameters were deposited with the Cambridge Crystallographic Data Centre (CCDC). The CCDC registry numbers and a brief summary of data collection and refinement are provided in Table A1 (Appendix A).

**Author Contributions:** Conceptualization, Ö.Ü., R.E. and M.S.; methodology, Ö.Ü., D.I., A.D.-A., S.Y., T.D., S.M.G. and M.S.; validation, Ö.Ü., D.I., A.D.-A., S.Y., T.D. and S.M.G.; formal analysis, Ö.Ü., A.D.-A., S.Y., T.D., S.M.G. and M.S.; investigation, Ö.Ü., D.I., A.D.-A., S.Y., T.D., S.M.G., G.D., M.J. and M.S.; resources, R.E. and M.S.; writing—original draft preparation, Ö.Ü., T.D. and M.S.; writing—review and editing, Ö.Ü., A.D.-A., S.M.G. and M.S.; visualization, Ö.Ü., A.D.-A. and T.D.; supervision, R.E. and M.S.; funding acquisition, R.E. and M.S. All authors have read and agreed to the published version of the manuscript.

**Funding:** This research was funded by the U.S. National Science Foundation (award CHE-1955754 to M.S.). G.D. and M.S. acknowledge support from the NSF Research Experiences for Undergraduates program (award CHE-1659661). The Rigaku Synergy-S single-crystal X-ray diffractometer used for crystallographic work was acquired through the NSF MRI program (award CHE-1828362).

**Institutional Review Board Statement:** Not applicable.

**Informed Consent Statement:** Not applicable.

**Data Availability Statement:** Data supporting reported results can be obtained upon request by emailing the corresponding author.

**Acknowledgments:** This research used resources provided by the X-ray Crystallography Center (FSU075000XRAY) and the Materials Characterization Laboratory (FSU075000MAC) at the FSU Department of Chemistry and Biochemistry.

**Conflicts of Interest:** The authors declare no conflict of interest.

## Appendix A

Table A1. Data collection and structure refinement parameters for complexes 1a, 1b, 2a and 2b.

Formula	FeCl <sub>2</sub> O <sub>8</sub> N <sub>8</sub> C <sub>24</sub> H <sub>28</sub> (1a)		FeF <sub>8</sub> N <sub>8</sub> C <sub>24</sub> B <sub>2</sub> H <sub>28</sub> (1b)		FeCl <sub>2</sub> O <sub>8</sub> N <sub>7</sub> C <sub>22</sub> H <sub>29</sub> S <sub>2</sub> (2a·CH <sub>3</sub> CN)		FeSF <sub>8</sub> N <sub>6</sub> C <sub>20</sub> B <sub>2</sub> H <sub>26</sub> S <sub>2</sub> (2b)	
T, K	90(1)	230(1)	100(1)	230(1)	100(1)	230(1)	100(1)	230(1)
CCDC number	1965486	1965490	1965488	1965489	1965484	1965491	1965485	1965487
Space group	<i>P</i> $\bar{1}$	<i>P</i> $\bar{1}$	<i>P</i> 2 <sub>1</sub> / <i>c</i>	<i>P</i> 2 <sub>1</sub> / <i>c</i>	<i>P</i> 2 <sub>1</sub> / <i>c</i>	<i>P</i> 2 <sub>1</sub> / <i>c</i>	<i>P</i> 2 <sub>1</sub> / <i>c</i>	<i>P</i> 2 <sub>1</sub> / <i>c</i>
<i>a</i> , Å	12.2975(3)	12.4579(7)	12.836(4)	13.348(3)	11.460(1)	11.594(3)	13.134(2)	13.135(2)
<i>b</i> , Å	13.6406(4)	13.8651(8)	17.474(6)	17.562(4)	20.491(2)	20.691(5)	17.169(3)	17.171(3)
<i>c</i> , Å	17.3808(5)	17.512(1)	15.887(4)	16.243(4)	12.484(1)	12.529(3)	14.335(2)	14.336(2)
$\alpha$ , deg	81.828(2)	82.266(5)						
$\beta$ , deg	77.321(5)	77.320(5)	129.56(2)	130.85(1)	108.122(1)	108.091(3)	125.200(9)	125.199(2)
$\gamma$ , deg	84.175(2)	84.248(5)						
<i>V</i> , Å <sup>3</sup>	2809.3(1)	2916.4(3)	2747(2)	2880(1)	2786.1(5)	2857(1)	2641.5(7)	2642.2(7)
<i>Z</i>	4	4	4	4	4	4	4	4
Crystal color	light yellow	light yellow	dark orange	orange	red	red	red	red
Crystal size, mm <sup>3</sup>	0.50 × 0.30 × 0.14	0.48 × 0.32 × 0.12	0.13 × 0.13 × 0.11	0.19 × 0.18 × 0.16	0.53 × 0.47 × 0.19	0.29 × 0.12 × 0.03	0.13 × 0.13 × 0.11	0.17 × 0.13 × 0.08
<i>d</i> <sub>calc</sub> , g/cm <sup>3</sup>	1.616	1.556	1.591	1.518	1.694	1.652	1.620	1.619
$\mu$ , mm <sup>-1</sup>	0.791	0.762	0.636	0.606	0.944	0.921	0.809	0.809
$\lambda$ , Å	0.71073	0.71073	0.71073	0.71073	0.71073	0.71073	0.71073	0.71073
2 $\theta$ <sub>max</sub> , deg	27.48	27.48	26.37	28.51	28.52	28.53	28.59	28.58
Total refls. ( <i>R</i> <sub>int</sub> )	39132 (0.052)	33276 (0.047)	26980 (0.148)	33221 (0.036)	31167 (0.019)	26075 (0.022)	28863 (0.030)	28869 (0.029)
Unique refls.	12690	13208	5568	6920	6667	6745	6309	6309
Parameters/Restraints	787/0	787/2	456/32	454/10	402/0	386/0	433/10	423/10
<i>R</i> <sub>1</sub> , <i>wR</i> <sub>2</sub> [ <i>I</i> > 2 $\sigma$ ( <i>I</i> )] <sup>a</sup>	0.069, 0.174	0.076, 0.206	0.072, 0.200	0.042, 0.120	0.037, 0.097	0.038, 0.106	0.051, 0.139	0.040, 0.101
<i>R</i> <sub>1</sub> , <i>wR</i> <sub>2</sub> (all data)	0.086, 0.186	0.108, 0.228	0.077, 0.204	0.064, 0.129	0.041, 0.098	0.050, 0.115	0.067, 0.151	0.056, 0.111
Goodness of fit <sup>b</sup>	1.031	1.023	1.095	1.041	1.130	1.032	1.067	1.084
Diff. peak/hole, e/Å <sup>3</sup>	1.60, −0.87	1.58, −0.50	1.59, −1.10	0.58, −0.49	0.51, −0.61	1.07, −0.50	0.95, −0.63	0.52, −0.42

<sup>a</sup>  $R_1 = \sum ||F_o| - |F_c|| / \sum |F_o|$ ;  $wR_2 = [\sum [w(F_o^2 - F_c^2)^2] / \sum [w(F_o^2)^2]]^{1/2}$ ; <sup>b</sup> Goodness-of-fit =  $[\sum [w(F_o^2 - F_c^2)^2] / (N_{obs} - N_{params})]^{1/2}$ , based on all data.

## References

1. Gütllich, P.; Goodwin, H.A. Spin crossover—An overall perspective. *Top. Curr. Chem.* **2004**, *233*, 1–47. [[CrossRef](#)]
2. Halcrow, M.A. The spin-states and spin-transitions of mononuclear iron(II) complexes of nitrogen-donor ligands. *Polyhedron* **2007**, *26*, 3523–3576. [[CrossRef](#)]
3. Lennartson, A.; Bond, A.D.; Piligkos, S.; McKenzie, C.J. Four-site cooperative spin crossover in a mononuclear Fe<sup>II</sup> Complex. *Angew. Chem. Int. Ed.* **2012**, *51*, 11049–11052. [[CrossRef](#)]
4. Lennartson, A.; Southon, P.; Sciortino, N.F.; Kepert, C.J.; Frandsen, C.; Morup, S.; Piligkos, S.; McKenzie, C.J. Reversible guest binding in a non-porous Fe<sup>II</sup> coordination polymer host toggles spin crossover. *Chem. Eur. J.* **2015**, *21*, 16066–16072. [[CrossRef](#)]
5. Arroyave, A.; Lennartson, A.; Dragulescu-Andrasi, A.; Pedersen, K.S.; Piligkos, S.; Stoian, S.A.; Greer, S.M.; Pak, C.; Hietsoi, O.; Phan, H.; et al. Spin crossover in Fe(II) complexes with N<sub>4</sub>S<sub>2</sub> coordination. *Inorg. Chem.* **2016**, *55*, 5904–5913. [[CrossRef](#)]
6. Hogue, R.W.; Feltham, H.L.C.; Miller, R.G.; Brooker, S. Spin crossover in dinuclear N<sub>4</sub>S<sub>2</sub> iron(II) thioether-triazole complexes: Access to [HS-HS], [HS-LS], and [LS-LS] states. *Inorg. Chem.* **2016**, *55*, 4152–4165. [[CrossRef](#)]
7. Yergeshbayeva, S.; Hrudka, J.J.; Lengyel, J.; Erkasov, R.; Stoian, S.A.; Dragulescu-Andrasi, A.; Shatruk, M. Heteroleptic Fe(II) complexes with N<sub>4</sub>S<sub>2</sub> coordination as a platform for designing spin-crossover materials. *Inorg. Chem.* **2017**, *56*, 11096–11103. [[CrossRef](#)]
8. Dragulescu-Andrasi, A.; Hietsoi, O.; Üngör, Ö.; Dunk, P.W.; Stubbs, V.; Arroyave, A.; Kovnir, K.; Shatruk, M. Dicyanometalates as building blocks for multinuclear iron(II) spin-crossover complexes. *Inorg. Chem.* **2019**, *58*, 11920–11926. [[CrossRef](#)]
9. Klokishner, S.; Reu, O. Modeling of spin crossover in iron(II) complexes with N<sub>4</sub>S<sub>2</sub> coordination. *J. Phys. Chem. C* **2019**, *123*, 19984–19990. [[CrossRef](#)]
10. Kawamura, A.; Xie, J.; Boyn, J.-N.; Jesse, K.A.; McNeece, A.J.; Hill, E.A.; Collins, K.A.; Valdez-Moreira, J.A.; Filatov, A.S.; Kurutz, J.W.; et al. Reversible switching of organic diradical character via iron-based spin-crossover. *J. Am. Chem. Soc.* **2020**, *142*, 17670–17680. [[CrossRef](#)]
11. Plaza-Lozano, D.; Conde-Gallardo, A.; Olguín, J. Spin crossover vs. high-spin iron(II) complexes in N<sub>4</sub>S<sub>2</sub> coordination sphere containing picolyl-thioether ligands and NCE (E=S, Se and BH<sub>3</sub>) co-ligands. *Eur. J. Inorg. Chem.* **2021**, *2021*, 2846–2856. [[CrossRef](#)]
12. Guionneau, P.; Marchivie, M.; Bravic, G.; Létard, J.F.; Chasseau, D. Structural aspects of spin crossover. Example of the [Fe<sup>II</sup>L<sub>n</sub>(NCS)<sub>2</sub>] complexes. *Top. Curr. Chem.* **2004**, *234*, 97–128. [[CrossRef](#)]
13. Phan, H.; Hrudka, J.J.; Igimbayeva, D.; Lawson Daku, L.M.; Shatruk, M. A simple approach for predicting the spin state of homoleptic Fe(II) tris-diimine complexes. *J. Am. Chem. Soc.* **2017**, *139*, 6437–6447. [[CrossRef](#)]
14. Matouzenko, G.S.; Bousseksou, A.; Lecocq, S.; van Koningsbruggen, P.J.; Perrin, M.; Kahn, O.; Collet, A. Spin transition in [Fe(DPEA)(NCS)<sub>2</sub>], a compound with the new tetradentate ligand (2-aminoethyl)bis(2-pyridylmethyl)amine (DPEA): Crystal structure, magnetic properties, and Mössbauer spectroscopy. *Inorg. Chem.* **1997**, *36*, 2975–2981. [[CrossRef](#)]
15. Phan, H.V.; Chakraborty, P.; Chen, M.M.; Calm, Y.M.; Kovnir, K.; Keniley, L.K.; Hoyt, J.M.; Knowles, E.S.; Besnard, C.; Meisel, M.W.; et al. Heteroleptic Fe<sup>II</sup> complexes of 2,2'-biimidazole and its alkylated derivatives: Spin-crossover and photomagnetic behavior. *Chem. Eur. J.* **2012**, *18*, 15805–15815. [[CrossRef](#)]
16. Li, B.; Wei, R.J.; Tao, J.; Huang, R.B.; Zheng, L.S.; Zheng, Z. Solvent-induced transformation of single crystals of a spin-crossover (SCO) compound to single crystals with two distinct SCO centers. *J. Am. Chem. Soc.* **2010**, *132*, 1558–1566. [[CrossRef](#)] [[PubMed](#)]
17. Wei, R.-J.; Tao, J.; Huang, R.-B.; Zheng, L.-S. Reversible and irreversible vapor-induced guest molecule exchange in spin-crossover compounds. *Inorg. Chem.* **2011**, *50*, 8553–8564. [[CrossRef](#)] [[PubMed](#)]
18. Abushamleh, A.S.; Goodwin, H.A. Coordination of 2,2'-biimidazole with iron, cobalt, nickel and copper. *Aus. J. Chem.* **1979**, *32*, 513–518. [[CrossRef](#)]
19. König, E.; Ritter, G.; Kulshreshtha, S.K.; Nelson, S.M. The high-spin (<sup>5</sup>T<sub>2</sub>) ↔ low-spin (<sup>1</sup>A<sub>1</sub>) transition in solid tris(2,2'-bi-2-imidazoline)iron(II) diperchlorate. Hysteresis effects, simultaneous change of spin and lattice characteristics, and order-disorder phenomena of the perchlorate anion. *Inorg. Chem.* **1982**, *21*, 3022–3029. [[CrossRef](#)]
20. Shatruk, M.; Dragulescu-Andrasi, A.; Chambers, K.E.; Stoian, S.A.; Bominaar, E.L.; Achim, C.; Dunbar, K.R. Properties of Prussian blue materials manifested in molecular complexes: Observation of cyanide linkage isomerism and spin-crossover behavior in pentanuclear cyanide clusters. *J. Am. Chem. Soc.* **2007**, *129*, 6104–6116. [[CrossRef](#)]
21. Chakraborty, P.; Enachescu, C.; Walder, C.; Bronisz, R.; Hauser, A. Thermal and light-induced spin switching dynamics in the 2D coordination network of {[Zn<sub>1-x</sub>Fe<sub>x</sub>(bbtr)<sub>3</sub>](ClO<sub>4</sub>)<sub>2</sub>]<sub>∞</sub>: The role of cooperative effects. *Inorg. Chem.* **2012**, *51*, 9714–9722. [[CrossRef](#)] [[PubMed](#)]
22. Shatruk, M.; Phan, H.; Chrisostomo, B.A.; Suleimenova, A. Symmetry-breaking structural phase transitions in spin crossover complexes. *Coord. Chem. Rev.* **2015**, *289*, 62–73. [[CrossRef](#)]
23. Gütllich, P.; Bill, E.; Trautwein, A.X. *Mössbauer Spectroscopy and Transition Metal Chemistry Fundamentals and Applications*; Springer: Berlin/Heidelberg, Germany, 2011.
24. Hauser, A. Light-induced spin crossover and the high-spin → low-spin relaxation. *Top. Curr. Chem.* **2004**, *234*, 155–198. [[CrossRef](#)]
25. Létard, J.F.; Asthana, S.; Shepherd, H.J.; Guionneau, P.; Goeta, A.E.; Suemura, N.; Ishikawa, R.; Kaizaki, S. Photomagnetism of a *sym-cis*-dithiocyanato iron(II) complex with a tetradentate *N,N'*-bis(2-pyridylmethyl)1,2-ethanediamine ligand. *Chem. Eur. J.* **2012**, *18*, 5924–5934. [[CrossRef](#)]

26. Kojima, T.; Leising, R.A.; Yan, S.; Que, L., Jr. Alkane functionalization at nonheme iron centers. Stoichiometric transfer of metal-bound ligands to alkane. *J. Am. Chem. Soc.* **1993**, *115*, 11328–11335. [[CrossRef](#)]
27. Lennartson, A.; McKenzie, C.J. 1,2-Bis[(pyridin-2-ylmethyl)sulfanyl]ethane and its dimorphic hydrochloride salt. *Acta Crystallogr. Sect. C* **2011**, *67*, 354–358. [[CrossRef](#)]
28. Forssel, G. Über die Einwirkung des Aethylendiamins auf Thioamide. I. *Ber. Deutsch. Chem. Gesell.* **1892**, *25*, 2132–2142. [[CrossRef](#)]
29. Bain, G.A.; Berry, J.F. Diamagnetic corrections and Pascal's constants. *J. Chem. Educ.* **2008**, *85*, 532–536. [[CrossRef](#)]
30. Prescher, C.; McCammon, C.; Dubrovinsky, L. MossA. A program for analyzing energy-domain Mössbauer spectra from conventional and synchrotron sources. *J. Appl. Crystallogr.* **2012**, *45*, 329–331. [[CrossRef](#)]
31. SMART and SAINT; Bruker AXS Inc.: Madison, WI, USA, 2007.
32. CrysAlis; Oxford Diffraction Ltd.: Abingdon, UK, 2006.
33. Sheldrick, G.M. SADABS; University of Göttingen: Göttingen, Germany, 1996.
34. Sheldrick, G.M. XPREP. *Space Group Determination and Reciprocal Space Plots*; Siemens Analytical X-ray Instruments: Madison, WI, USA, 1991.
35. Sheldrick, G.M. Crystal structure refinement with SHELXL. *Acta Crystallogr. Sect. C* **2015**, *71*, 3–8. [[CrossRef](#)]